A Third-Order Upwind Compact Scheme on Curvilinear Meshes for the Incompressible Navier-Stokes Equations

Abdullah Shah[1,2], Hong Guo[1] and Li Yuan[1,*]

[1] *LSEC, Institute of Computational Mathematics and Scientific/Engineering Computing, Academy of Mathematics and Systems Science, Chinese Academy of Sciences, Beijing 100080, China.*
[2] *Department of Mathematics, COMSATS Institute of Information Technology, Islamabad, Pakistan.*

Abstract. This paper presents a new version of the upwind compact finite difference scheme for solving the incompressible Navier-Stokes equations in generalized curvilinear coordinates. The artificial compressibility approach is used, which transforms the elliptic-parabolic equations into the hyperbolic-parabolic ones so that flux difference splitting can be applied. The convective terms are approximated by a third-order upwind compact scheme implemented with flux difference splitting, and the viscous terms are approximated by a fourth-order central compact scheme. The solution algorithm used is the Beam-Warming approximate factorization scheme. Numerical solutions to benchmark problems of the steady plane Couette-Poiseuille flow, the lid-driven cavity flow, and the constricting channel flow with varying geometry are presented. The computed results are found in good agreement with established analytical and numerical results. The third-order accuracy of the scheme is verified on uniform rectangular meshes.

AMS subject classifications: 76D05, 65N06

Key words: Upwind compact difference, flux difference splitting, incompressible Navier-Stokes equations, artificial compressibility, lid-driven cavity flow.

1 Introduction

The incompressible Navier-Stokes (N-S) equations are fundamental equations in fluid mechanics. Accurate numerical solution to these equations plays an important role in

---

*Corresponding author. *Email addresses:* `abdullah@lsec.cc.ac.cn` (A. Shah), `guoh@lsec.cc.ac.cn` (H. Guo), `lyuan@lsec.cc.ac.cn` (L. Yuan)

many applications. In the development of appropriate computational approaches to tackle challenging areas like direct numerical and large-eddy simulation of turbulence, high-order methods are preferable over standard second-order formulations. In the category of high-order methods, the compact difference scheme represents an attractive choice because it uses smaller stencils and gives better resolution at high wave-numbers than non-compact schemes of the same order [1–4].

The compact schemes can generally be classified into two categories: central and upwind. Central compact schemes are non-dissipative, and using central compact schemes on non-staggered meshes for convection terms might cause numerical oscillations even for flows without discontinuities. Reducing or removing such oscillations requires the use of artificial dissipation or filtering [5]. On the other hand, upwind compact schemes with dissipative properties are more stable. Fu and Ma [6,7], and among others [8–10] have developed some upwind compact schemes. Using these schemes for convective terms can provide grid-scale linkage for each variable to avoid odd-even decoupling, and in principle can prevent non-physical oscillations in smooth regions.

We note that one advantage of the upwind compact scheme by Fu and Ma [6,7] lies in that, the implicit part involves only two points rather than more points as most other upwind compact schemes do [10]. This will reduce the computational cost.

Upwind compact schemes for conservation laws require appropriate split fluxes being used. Flux vector splitting is most widely used. But fewer attempts have been made to use flux difference splitting (FDS) [11] in conjunction with upwind compact schemes. In fact, FDS is suitable for more general situations and is less dissipative than other general splitting like Lax-Friedrichs splitting. It is applicable to incompressible flows when the artificial compressibility (AC) approach is adopted. The equations for steady incompressible viscous flows with the AC formulation are (see [12])

$$\frac{\partial p}{\partial \tau} + \beta \nabla \cdot \mathbf{u} = 0, \tag{1.1a}$$

$$\frac{\partial \mathbf{u}}{\partial \tau} + \mathbf{u} \cdot \nabla \mathbf{u} + \nabla p - \frac{1}{Re} \nabla^2 \mathbf{u} = 0, \tag{1.1b}$$

where β is the artificial compressibility parameter and τ is a pseudo-time (or iteration parameter). Since the inviscid version of the above equations are hyperbolic, upwind differences can be applied. Corresponding solution methods can be time marching ones borrowed from compressible solvers. As the solution converges, the time derivative of pressure approaches zero and the incompressibility is satisfied.

One of the disadvantages of the AC approach is the selection of the artificial compressibility parameter β. The optimum β for achieving fastest convergence is problem dependent. Through trial runs on coarse meshes, the optimum β can be found, and subsequent steady-state problems can be solved efficiently. But the AC approach is neither efficient nor accurate for time-dependent problems if sub-iteration is not converged quickly and fully. In spite of the drawbacks, numerous studies which utilized the AC approach for solving steady-state and time-dependent incompressible flow problems were

conducted in the past three decades, see, Kwak and Rogers [13,14], and others [15–17].

In this paper, we extend a class of high-order upwind compact difference schemes [6,7] to numerical solutions of the incompressible N-S equations with the AC approach. The peculiarity of the present extension is that the explicit part of the upwind compact scheme is computed based on FDS. Because Rogers et al. [13,14] already used FDS in conventional third-order upwind schemes, the present scheme can be viewed as a compact scheme version. The accuracy of the present scheme was verified through several two-dimensional benchmark problems.

This paper is organized as follows. In the next section, the governing equations and their formulation for the artificial compressibility approach in curvilinear coordinates are given. Section 3 describes the space discretization including the upwind compact scheme to approximate the convective terms and solution method to the discretized equations. Numerical results for several 2D test problems are presented in Sections 4 and 5. Section 6 concludes this paper.

2   Governing equations

Starting from the 2D non-dimensional incompressible N-S equations in general curvilinear coordinates (ξ,η) with the artificial compressibility term (assuming a stationary coordinates, $\xi = \xi(x,y)$, $\eta = \eta(x,y)$, such that the Jacobian of transformation and other metrics are time independent, see [14])

$$\frac{\partial \hat{\mathbf{Q}}}{\partial \tau} + \frac{\partial (\hat{\mathbf{E}} - \hat{\mathbf{E}}_v)}{\partial \xi} + \frac{\partial (\hat{\mathbf{F}} - \hat{\mathbf{F}}_v)}{\partial \eta} = 0, \tag{2.1}$$

where

$$\hat{\mathbf{Q}} = \frac{\mathbf{Q}}{J} = \frac{1}{J} \begin{bmatrix} p \\ u \\ v \end{bmatrix}, \quad \hat{\mathbf{E}} = \frac{1}{J} \begin{bmatrix} \beta U \\ uU + \xi_x p \\ vU + \xi_y p \end{bmatrix}, \quad \hat{\mathbf{F}} = \frac{1}{J} \begin{bmatrix} \beta V \\ uV + \eta_x p \\ vV + \eta_y p \end{bmatrix},$$

$$\hat{\mathbf{E}}_v = \frac{1}{\mathrm{Re}J} \begin{bmatrix} 0 \\ \left(\xi_x^2 + \xi_y^2\right) u_\xi + \left(\xi_x \eta_x + \xi_y \eta_y\right) u_\eta \\ \left(\xi_x^2 + \xi_y^2\right) v_\xi + \left(\xi_x \eta_x + \xi_y \eta_y\right) v_\eta \end{bmatrix},$$

$$\hat{\mathbf{F}}_v = \frac{1}{\mathrm{Re}J} \begin{bmatrix} 0 \\ \left(\xi_x \eta_x + \xi_y \eta_y\right) u_\xi + \left(\eta_x^2 + \eta_y^2\right) u_\eta \\ \left(\xi_x \eta_x + \xi_y \eta_y\right) v_\xi + \left(\eta_x^2 + \eta_y^2\right) v_\eta \end{bmatrix},$$

$$U = \xi_x u + \xi_y v, \quad V = \eta_x u + \eta_y v,$$

U and V are the contra-variant velocity components in curvilinear coordinate directions, ξ and η, respectively, $\hat{\mathbf{E}}$ and $\hat{\mathbf{F}}$ are the inviscid fluxes, $\hat{\mathbf{E}}_v$ and $\hat{\mathbf{F}}_v$ are the viscous fluxes, *Re*

is the Reynolds number and the Jacobian determinant of transformation is defined as

$$J = \left| \frac{\partial(\xi,\eta)}{\partial(x,y)} \right| = \left| \frac{\partial(x,y)}{\partial(\xi,\eta)} \right|^{-1} = \left| \begin{array}{cc} x_\xi & x_\eta \\ y_\xi & y_\eta \end{array} \right|^{-1}.$$

Other metrics are

$$\frac{\xi_x}{J} = y_\eta, \quad \frac{\xi_y}{J} = -x_\eta, \quad \frac{\eta_x}{J} = -y_\xi, \quad \frac{\eta_y}{J} = x_\xi.$$

The inviscid flux for both Cartesian and curvilinear coordinates, and for any direction, can be uniformly written as

$$\hat{\mathbf{E}}_k = \hat{k}_x \mathbf{E} + \hat{k}_y \mathbf{F} = \hat{k}_x \left[\begin{array}{c} \beta u \\ u^2 + p \\ vu \end{array} \right] + \hat{k}_y \left[\begin{array}{c} \beta v \\ uv \\ v^2 + p \end{array} \right] = \left[\begin{array}{c} \beta \Theta \\ u\Theta + \hat{k}_x p \\ v\Theta + \hat{k}_y p \end{array} \right]. \tag{2.2}$$

The Jacobian matrix of this flux vector is

$$\mathbf{A}_k = \frac{\partial \hat{\mathbf{E}}_k}{\partial \mathbf{Q}} = \left[\begin{array}{ccc} 0 & \hat{k}_x \beta & \hat{k}_y \beta \\ \hat{k}_x & \hat{k}_x u + \Theta & \hat{k}_y u \\ \hat{k}_y & \hat{k}_x v & \hat{k}_y v + \Theta \end{array} \right], \tag{2.3}$$

where $\Theta = \hat{k}_x u + \hat{k}_y v$, $(\hat{k}_x, \hat{k}_y) = (k_x, k_y)/J$, $k = \xi, \eta$.

Notice that $\hat{k}_x = 1$, $\hat{k}_y = 0$, and $\hat{k}_x = 0$, $\hat{k}_y = 1$ give $\mathbf{E}$ and $\mathbf{F}$ in Cartesian coordinates respectively. A similarity transformation for the Jacobian matrix is

$$\mathbf{A}_k = \mathbf{T}_k \mathbf{\Lambda}_k \mathbf{T}_k^{-1}, \tag{2.4}$$

with eigenvalue matrix $\mathbf{\Lambda}_k = \mathrm{diag}(\Theta, \Theta + c, \Theta - c)$, where c is the scaled artificial speed of sound given by

$$c = \sqrt{\Theta^2 + \beta(\hat{k}_x^2 + \hat{k}_y^2)}.$$

The right and left eigenvector matrices are

$$\mathbf{T}_k = \left[\begin{array}{ccc} 0 & -\tilde{c}(\tilde{\Theta} - \tilde{c}) & \tilde{c}(\tilde{\Theta} + \tilde{c}) \\ \tilde{k}_y & u - \tilde{k}_x(\tilde{\Theta} - \tilde{c}) & u - \tilde{k}_x(\tilde{\Theta} + \tilde{c}) \\ -\tilde{k}_x & v - \tilde{k}_y(\tilde{\Theta} - \tilde{c}) & v - \tilde{k}_y(\tilde{\Theta} + \tilde{c}) \end{array} \right], \tag{2.5a}$$

$$\mathbf{T}_k^{-1} = \frac{1}{\tilde{c}^2} \left[\begin{array}{cccc} \tilde{k}_x v - \tilde{k}_y u & v\tilde{\Theta} + \tilde{k}_y \beta & -(u\tilde{\Theta} + \tilde{k}_x \beta) \\ \frac{1}{2} & \frac{1}{2}\tilde{k}_x(\tilde{\Theta} + \tilde{c}) & \frac{1}{2}\tilde{k}_y(\tilde{\Theta} + \tilde{c}) \\ \frac{1}{2} & \frac{1}{2}\tilde{k}_x(\tilde{\Theta} - \tilde{c}) & \frac{1}{2}\tilde{k}_y(\tilde{\Theta} - \tilde{c}) \end{array} \right], \tag{2.5b}$$

where

$$\tilde{k}_x = \frac{\hat{k}_x}{\sqrt{\hat{k}_x^2 + \hat{k}_y^2}}, \quad \tilde{\Theta} = \frac{\Theta}{\sqrt{\hat{k}_x^2 + \hat{k}_y^2}}, \quad \tilde{c} = \frac{c}{\sqrt{\hat{k}_x^2 + \hat{k}_y^2}}.$$

3   Numerical scheme

3.1   Spatial differences

An upwind compact scheme is used to discretize the convective terms. Because of the hyperbolic nature, the convective terms in Eq. (2.1) can be split into positive and negative parts:

$$\partial_\xi \hat{\mathbf{E}} = \left(\hat{\mathbf{E}}_\xi\right)^+ + \left(\hat{\mathbf{E}}_\xi\right)^-, \tag{3.1}$$

which approximate the derivatives of positively traveling and negatively traveling waves, respectively. These derivatives can be obtained by using the third-order upwind compact scheme developed by Fu and Ma [6,7]:

$$\frac{2}{3}\left(\hat{\mathbf{E}}_\xi\right)_i^+ + \frac{1}{3}\left(\hat{\mathbf{E}}_\xi\right)_{i-1}^+ = \frac{5\bigtriangledown_i \hat{\mathbf{E}}^+ + \bigtriangleup_i \hat{\mathbf{E}}^+}{6\Delta\xi} + \mathcal{O}(\Delta\xi^3), \tag{3.2a}$$

$$\frac{2}{3}\left(\hat{\mathbf{E}}_\xi\right)_i^- + \frac{1}{3}\left(\hat{\mathbf{E}}_\xi\right)_{i+1}^- = \frac{\bigtriangledown_i \hat{\mathbf{E}}^- + 5\bigtriangleup_i \hat{\mathbf{E}}^-}{6\Delta\xi} + \mathcal{O}(\Delta\xi^3), \tag{3.2b}$$

where $\bigtriangleup_i f = f_{i+1} - f_i$ and $\bigtriangledown_i f = f_i - f_{i-1}$. Eq. (3.2a) is explicitly marched forward and Eq. (3.2b) is marched backward to get all the derivatives once the right-hand side (RHS) and the boundary derivatives are given. Instead of computing the RHS from point-wise $\hat{\mathbf{E}}_i^\pm$ values as did in [6,7], we compute the RHS by FDS. Since each RHS term of Eqs. (3.2a)-(3.2b) can be viewed as the difference of split fluxes between neighboring points, it can be computed from FDS [11,14]:

$$\hat{\mathbf{E}}_{i+1}^\pm - \hat{\mathbf{E}}_i^\pm \equiv \bigtriangleup\hat{\mathbf{E}}_{i+\frac{1}{2}}^\pm = \mathbf{A}^\pm(\overline{\mathbf{Q}})\left(\mathbf{Q}_{i+1} - \mathbf{Q}_i\right), \tag{3.3}$$

where $\bigtriangleup\hat{\mathbf{E}}_{i+1/2}^\pm$ is the flux difference across positive or negative traveling waves. The split Jacobian matrix $\mathbf{A}^\pm$ is evaluated using some intermediate value $\overline{\mathbf{Q}}$ which is a function of the surrounding points, $\mathbf{Q}_i$ and $\mathbf{Q}_{i+1}$. The Roe properties [11] which are necessary for a conservative scheme, are satisfied if $\overline{\mathbf{Q}}$ is taken as the arithmetic average of the surrounding points for incompressible flows [14]

$$\overline{\mathbf{Q}} = \frac{1}{2}\left(\mathbf{Q}_{i+1} + \mathbf{Q}_i\right).$$

This can be verified from Eqs. (2.2) and (2.3) if the metrics are frozen. To close the scheme, a second-order boundary scheme is used:

$$\left(\mathbf{E}_\xi\right)_i^+ = \frac{3\bigtriangleup\mathbf{E}_{i+\frac{1}{2}}^+ - \bigtriangleup\mathbf{E}_{i+\frac{3}{2}}^+}{2\Delta\xi} + \mathcal{O}(\Delta\xi^2) \ \text{ at the left boundary point;} \tag{3.4a}$$

$$\left(\mathbf{E}_\xi\right)_i^- = \frac{3\bigtriangleup\mathbf{E}_{i-\frac{1}{2}}^- - \bigtriangleup\mathbf{E}_{i-\frac{3}{2}}^-}{2\Delta\xi} + \mathcal{O}(\Delta\xi^2) \ \text{ at the right boundary point.} \tag{3.4b}$$

The viscous terms contain second derivatives of velocity components and first derivatives of velocity components and of metric coefficients. For simplicity and consistency with a third-order upwind compact scheme, second derivatives are approximated with a fourth-order central compact scheme supplemented by a conventional second-order central scheme near boundaries. First derivatives are computed with compact fourth-order central and biased schemes at inner points and boundary points, respectively. Analytical metrics are used whenever possible.

3.2 Solution scheme

Applying backward difference to the pseudo-time derivative, we obtain

$$\frac{1}{J}\frac{\Delta \mathbf{Q}^m}{\Delta \tau}+\left[\frac{\partial(\hat{\mathbf{E}}-\hat{\mathbf{E}}_v)}{\partial \xi}+\frac{\partial(\hat{\mathbf{F}}-\hat{\mathbf{F}}_v)}{\partial \eta}\right]^{m+1}=0, \tag{3.5}$$

where $\Delta \mathbf{Q}^m = \mathbf{Q}^{m+1} - \mathbf{Q}^m$, m refers to pseudo-time level.

Terms at $m+1$ level are linearized w.r.t. m level by using Taylor expansion, i.e.,

$$\hat{\mathbf{E}}^{m+1}\approx \hat{\mathbf{E}}^m+\left(\frac{\partial \hat{\mathbf{E}}}{\partial \mathbf{Q}}\right)^m(\mathbf{Q}^{m+1}-\mathbf{Q}^m)=\hat{\mathbf{E}}^m+\mathbf{A}^m\Delta \mathbf{Q}^m, \tag{3.6a}$$

$$\hat{\mathbf{E}}_v^{m+1}\approx \hat{\mathbf{E}}_v^m+\left(\frac{\partial \hat{\mathbf{E}}_v}{\partial \mathbf{Q}}\right)^m(\mathbf{Q}^{m+1}-\mathbf{Q}^m)=\hat{\mathbf{E}}_v^m+\mathbf{A}_v^m\Delta \mathbf{Q}^m. \tag{3.6b}$$

Thus we obtain the so-called delta form (solution for incremental variables $\Delta \mathbf{Q}$)

$$\left\{\mathbf{I}+\Delta \tau J\left[\frac{\partial(\mathbf{A}-\mathbf{A}_v)}{\partial \xi}+\frac{\partial(\mathbf{B}-\mathbf{B}_v)}{\partial \eta}\right]\right\}^m\Delta \mathbf{Q}^m$$
$$=-\Delta \tau J\left(\frac{\partial \hat{\mathbf{E}}}{\partial \xi}+\frac{\partial \hat{\mathbf{F}}}{\partial \eta}-\frac{\partial \hat{\mathbf{E}}_v}{\partial \xi}-\frac{\partial \hat{\mathbf{F}}_v}{\partial \eta}\right)^m$$
$$=-\mathbf{R}^m. \tag{3.7}$$

For factorization purpose, we will only retain the orthogonal parts of the viscous Jacobian matrices $\mathbf{A}_v$ and $\mathbf{B}_v$. The orthogonal parts of the viscous Jacobian matrices are

$$\mathbf{A}_v'=\left(\frac{1}{ReJ}\nabla \xi \cdot \nabla \xi\right)\mathbf{I}_m\frac{\partial}{\partial \xi}=\gamma_1\mathbf{I}_m\frac{\partial}{\partial \xi}, \tag{3.8a}$$

$$\mathbf{B}_v'=\left(\frac{1}{ReJ}\nabla \eta \cdot \nabla \eta\right)\mathbf{I}_m\frac{\partial}{\partial \eta}=\gamma_2\mathbf{I}_m\frac{\partial}{\partial \eta}, \tag{3.8b}$$

where $\mathbf{I}_m=\text{diag}\,(0,1,1)$. The Beam-Warming approximate factorization (AF) scheme [18] applied to Eq. (3.7) can be symbolically written as

$$\pounds_\xi \pounds_\eta \cdot \Delta \mathbf{Q}^m=-\mathbf{R}^m. \tag{3.9}$$

To obtain block tri-diagonal equations, the convective terms in LHS of Eq. (3.9) are discretized by 1st-order upwind difference and viscous terms by 2nd-order central difference, e.g.,

$$\triangle_\xi f = \frac{f_{i+1} - f_i}{\Delta \xi}, \quad \nabla_\xi f = \frac{f_i - f_{i-1}}{\Delta \xi},$$

$$\delta_\xi \gamma_1 \delta_\xi f = \frac{\gamma_{1_{i+1/2}}(f_{i+1} - f_i) - \gamma_{1_{i-1/2}}(f_i - f_{i-1})}{\Delta \xi^2}.$$

Note that the third-order upwind compact scheme and the fourth-order central scheme are still used for the RHS of Eq. (3.9). Thus we obtain the AF scheme in the form

$$\left[\mathbf{I} + \Delta \tau J \left(\nabla_\xi \mathbf{A}^+ + \triangle_\xi \mathbf{A}^- - \delta_\xi \gamma_1 \mathbf{I}_m \delta_\xi\right)\right]$$
$$\times \left[\mathbf{I} + \Delta \tau J \left(\nabla_\eta \mathbf{B}^+ + \triangle_\eta \mathbf{B}^- - \delta_\eta \gamma_2 \mathbf{I}_m \delta_\eta\right)\right] \Delta \mathbf{Q}^m = -\mathbf{R}^m, \qquad (3.10)$$

which requires solving block-tridiagonal equations.

To simplify further, the split Jacobian matrices of the flux vectors in the LHS are approximately constructed by

$$\mathbf{A}^\pm = \frac{1}{2}[\mathbf{A} \pm \rho(\mathbf{A})\mathbf{I}], \qquad (3.11)$$

where

$$\rho(\mathbf{A}) = \kappa \max[|\lambda(\mathbf{A})|],$$

with $\lambda(\mathbf{A})$ being the eigenvalues of the matrix $\mathbf{A}$, and κ a constant that is greater than or equal to unity ($\kappa = 1$ was used throughout this study).

4   Accuracy test

The modified lid driven cavity flow problem proposed by Shih *et al.* [19] has an exact solution for the N-S equations and is selected to study the order of accuracy of the present upwind compact scheme. The modifications include a lid velocity that varies along the upper lid of the cavity, i.e., $u(x,1) = 16(x^2 - 2x^3 + x^4)$, and a space-dependent body force $b(x,y,Re)$ in the y-direction within the cavity. The fact that $u(0,1) = 0$ and $u(1,1) = 0$, eliminate the singularity that exists at the top two corners of the classical lid driven cavity problem. The steady state problem was solved over a square domain $0 \leq x \leq 1$, $0 \leq y \leq 1$ by starting from arbitrary initial conditions (zero pressure and zero velocity) and with Dirichlet boundary condition for pressure and non-slip boundary condition for velocity
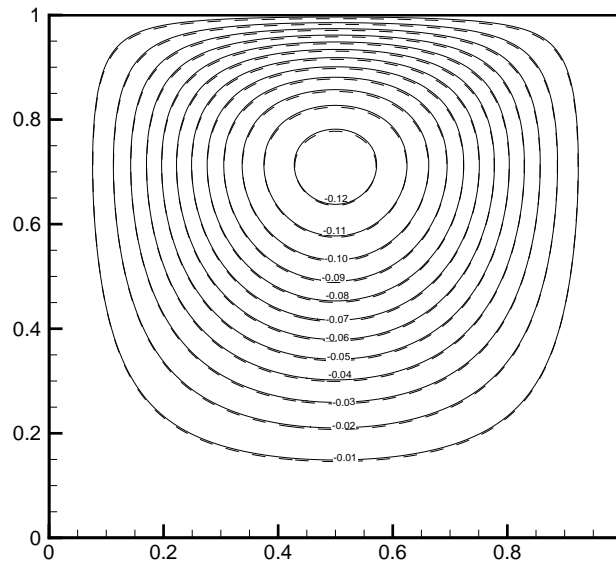
Figure 1: Streamlines for the modified lid driven cavity flow at $Re=1$.

on all boundaries. The exact solution of the problem is given in [19,20], which is

$$u(x,y) = 8\left(x^2 - 2x^3 + x^4\right)\left(-2y + 4y^3\right),$$

$$v(x,y) = -8\left(2x - 6x^2 + 4x^3\right)\left(-y^2 + y^4\right),$$

$$p(x,y,Re) = \frac{8}{Re}\left[\left(8x^3 - 12x^4 + \frac{24}{5}x^5\right)y + \left(2x - 6x^2 + 4x^3\right)\left(-2y + 4y^3\right)\right]$$

$$+ 64\left(\frac{x^4}{2} - 2x^5 + 3x^6 - 2x^7 + \frac{x^8}{2}\right)\left[-\left(-2y + 4y^3\right)^2 + \left(-2 + 12y^2\right)\left(-y^2 + y^4\right)\right],$$

$$b(x,y,Re) = -\frac{8}{Re}\left[\left(8x^3 - 12x^4 + \frac{24}{5}x^5\right) + \left(2x - 6x^2 + 4x^3\right)\left(-4 + 24y^2\right) + \right.$$

$$\left.\left(-12 + 24x\right)\left(-y^2 + y^4\right)\right] - 64\left\{0.5\left[\left(x^2 - 2x^3 + x^4\right)^2\left(-4y + 8y^3 - 24y^5\right)\right]\right.$$

$$\left. - \left(2y^3 - 6y^5 + 4y^7\right)\left(-2x^2 + 8x^3 - 14x^4 + 12x^5 - 4x^6\right)\right\}.$$

The computed streamlines are compared with the analytical ones for $Re=1$ in Fig. 1. We can see both are nearly identical.

Table 1 gives grid refinement results where the order of accuracy is calculated by

$$\mathcal{O}(A) = \frac{\log(e_2/e_1)}{\ln 2}.$$

Here $e_1 = |\phi_e - \phi_f|$, $e_2 = |\phi_e - \phi_c|$, ϕ_e, ϕ_f and ϕ_c stand for exact solution, solution on a fine grid and solution on a coarse grid with half of the points in each directions, respectively. This table clearly demonstrates that the order of accuracy for the present scheme is approximately 3.0.

Table 1: Grid refinement study for the modified driven cavity flow problem.

Grid	Re=1		Re=50		Re=100	
−	L$_2$ error	Order	L$_2$ error	Order	L$_2$ error	Order
11×11	1.85×10^{-3}	−	9.46×10^{-3}	−	1.35×10^{-2}	−
21×21	2.32×10^{-4}	3.0	1.21×10^{-3}	2.97	1.70×10^{-3}	2.99
41×41	2.58×10^{-5}	3.17	1.45×10^{-4}	3.06	2.07×10^{-4}	3.04
81×81	2.83×10^{-6}	3.19	1.69×10^{-5}	3.10	2.55×10^{-5}	3.02
161×161	3.17×10^{-7}	3.16	1.94×10^{-6}	3.12	3.15×10^{-6}	3.02

5   Numerical examples

The present numerical method was tested in several benchmark problems for the steady plane Couette-Poiseuille flow, the classical lid-driven cavity flow and the constricting channel flow. In the last problem curvilinear meshes were used.

5.1   The plane Couette-Poiseuille flow

The first test problem is the plane Couette-Poiseuille flow (e.g. [21]). The governing equations and the boundary conditions for the dependent variables $u = u(y)$ in dimensionless form are:

$$\left. \begin{array}{l} \Pi + \dfrac{d^2u}{dy^2} = 0 \\[2mm] u(y=0) = 0 \\[1mm] u(y=1) = 1 \end{array} \right\}, \tag{5.1}$$

where $\Pi = \frac{h^2}{\mu U_{\text{top}}} \frac{\Delta p}{\Delta L} \left(\frac{\Delta p}{\Delta L} = -\frac{\partial p}{\partial x} \text{ is a constant pressure gradient} \right)$ is a dimensionless number which can be interpreted as the ratio of the driving pressure gradient to the driving velocity of the upper plate. The exact solution to (5.1) is $u = \Pi/2(y - y^2) + y$.

The boundary conditions are as follows. Zero normal pressure gradient and non-slip velocity are used on the upper and lower plates. Pressure at the exit is prescribed to be zero and pressure at the inlet is specified a value according to Π, and zero gradient for velocities is imposed at both the inlet and the outlet. Fig. 2 shows the computed velocity profile for different Π values. The computational grid used has 65×65 uniform mesh points. It can be seen that the computational result agrees very well with the analytical solution. The numerical error is found to be below 10^{-14}, which is machine accuracy.

Fig. 3 shows the convergence history for different values of artificial compressibility factor β. The best value of β for which convergence is fastest is observed to be about 200. However, it must be emphasized that this optimal β is problem dependent. Although the convergence rate depends on β, it seems not a big problem as there is a wide range of β for which essentially same convergence rate can be obtained, e.g., for $10 < \beta < 1000$ in
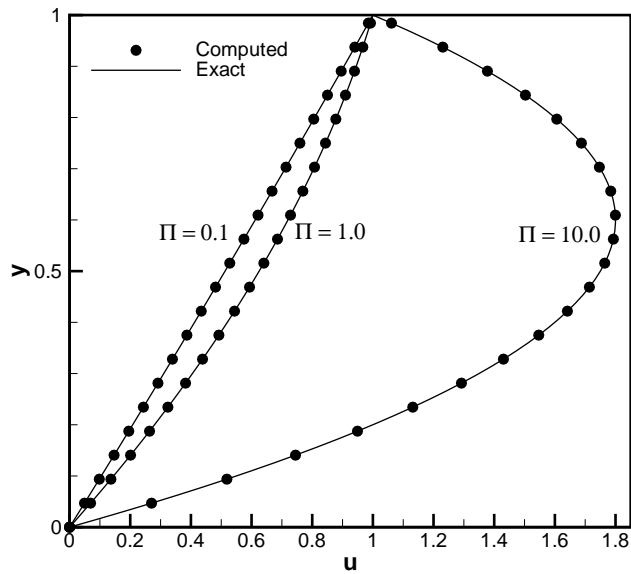
Figure 2: Velocity profile for the Couette-Poiseuille flow.
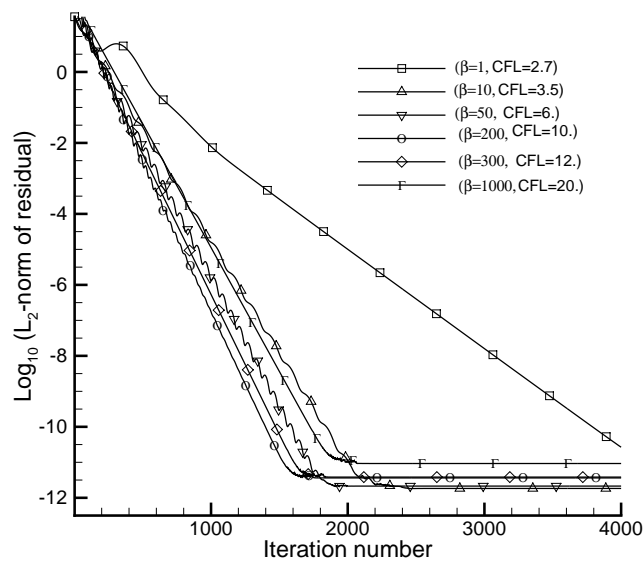

Figure 3: Convergence history for different values of β (with corresponding optimal CFL number) for the Couette-Poiseuille flow with $\Pi = 1.0$

this problem. It is also found that the optimal β and CFL number are not sensitive to grid size, therefore it is suggested that one first finds the optimal β (and corresponding CFL) on coarse meshes before conducting intensive calculations on fine meshes.

5.2   The lid driven cavity flow

The two-dimensional lid driven square cavity flow whose top wall moves with a uniform velocity, is frequently used as a benchmark problem for the assessment of numerical methods for the incompressible N-S equations, because the geometry as well as the boundary condition is very simple yet the flow phenomenon can be quite complicated. The top moving wall generates vorticity which diffuses into the cavity and this diffusion becomes the driven mechanism of the flow patterns. Since for $5,000 < Re < 15,000$, the flow becomes time periodic and for $15,000 \le Re \le 20,000$ it becomes chaotic [22], we only computed several Reynolds numbers ranging form 100 to 5000 for obtaining stationary solutions. The artificial compressibility factor β is found to have little effects on steady-state solutions, and we will show results for $\beta = 1$ and a 129×129 grid. Fig. 4 shows comparisons of the present $u-$ and $v-$ velocity components on the lines passing through the geometric center of the cavity along the $y-$ and $x-$ axis, respectively, with the calculations of Ghia [23]. Note that the origin of these plots is shifted for each successive Reynolds number case. We can see the present numerical results agree well with available results of [22–25].
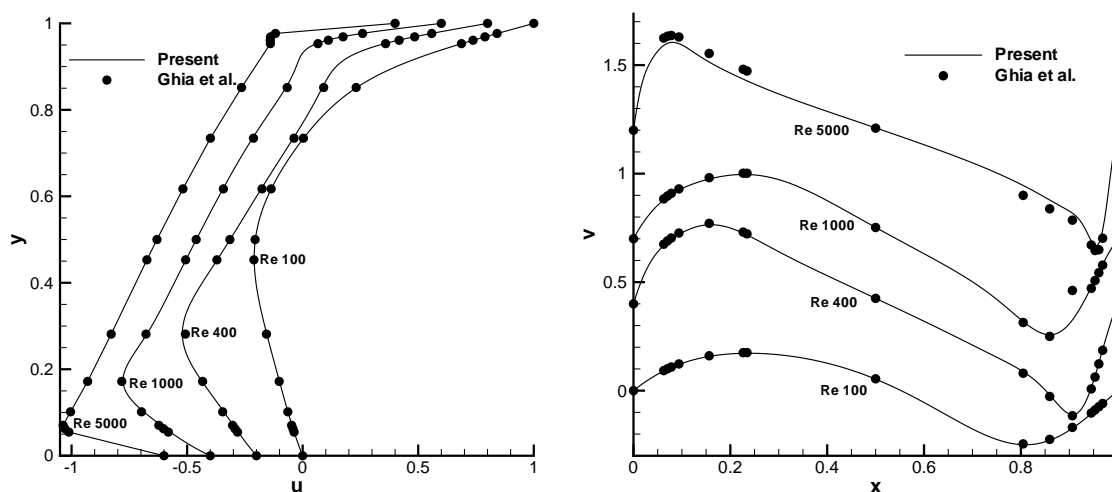

Figure 4: Comparison of u and v-velocity components for Re=100,400,1000 and 5000 with the computation of Ghia et al. [23].

In Fig. 5, the streamline contours for four Reynolds numbers: $Re = 100,400,1000,5000$, respectively, show the ability of our flow solver to predict the primary, secondary and particularly, tertiary vortices at higher Reynolds numbers. The secondary vortices formed at the bottom left and right corners are not equal to each other in size as the vortex at the bottom right corner is larger than at the bottom left corner. The streamline patterns are similar to those of [23, 25].

Fig. 6 shows comparison of the vorticity contours at Reynolds number 100 as computed from the velocity field. The contour lines are smooth, and the shape and positions
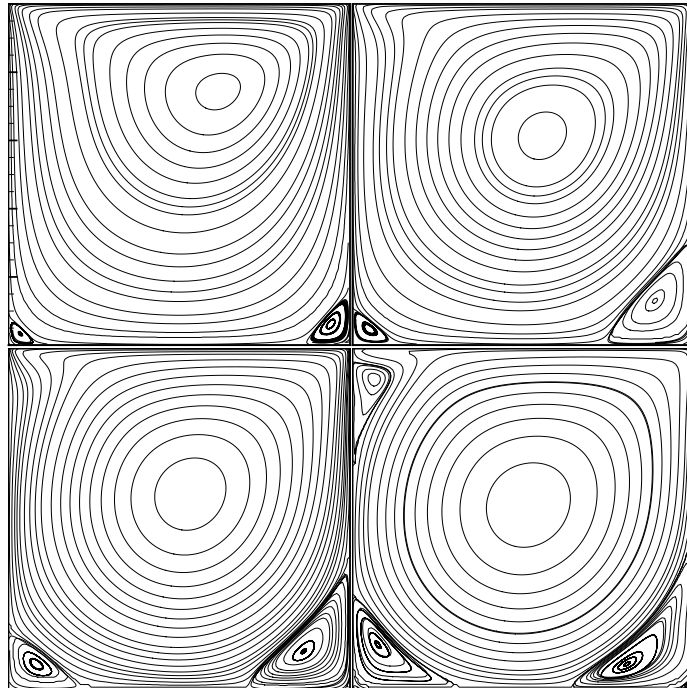
Figure 5: Streamlines showing the driven cavity flow at $Re=100,400,1000,5000$ respectively on a 129×129 grid.

of the contour lines are in good agreement with the results of [23].

The static pressure coefficient is defined as $C_p=2Re(P-P_{\text{ref}})$, where P_{ref} is the reference pressure at the middle of the lower wall. The contours of the static pressure coefficient at different Reynolds numbers were compared with that results given in [24] and we have seen a very good agreement between them. Since the upper wall velocity was chosen in the opposite direction in [24], we observed a very good symmetry between the two results as shown in Fig. 7 for the case of Reynolds number 100.

5.3 Constricting channel flow

Finally, we will test our scheme on curvilinear meshes using the laminar incompressible flow in a two-dimensional constricting channel, which has been studied numerically in [26–28]. As shown in Fig. 8, the channel boundary can be varied from a smooth constriction to one possessing a very sharp but a smooth corner through a controlled parameter δ. Different values of δ gives different channel geometries as shown in Fig. 9. The basic challenge in simulating this flow problem is to obtain the recirculation region immediately downstream of the corner for moderately high Reynolds numbers. The channel is symmetric about the centerline, therefore we only consider the upper half plane.

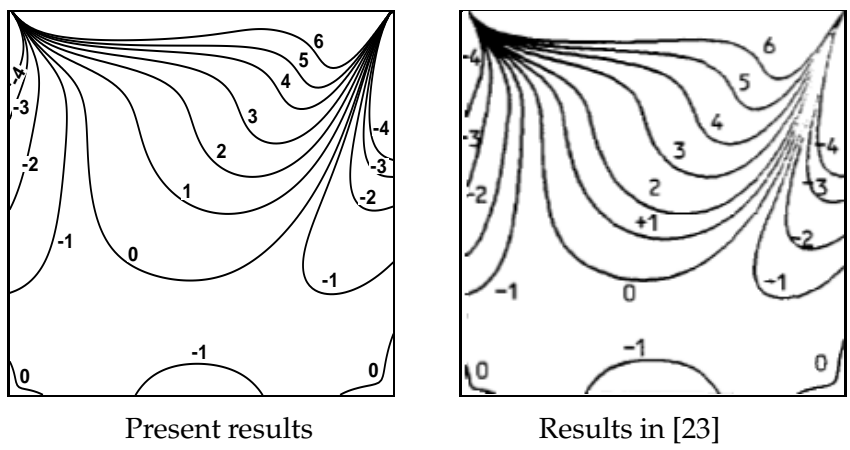To avoid high-frequency errors at the sharp corner, a large number of grid points are

Present results   Results in [23]

Figure 6: Vorticity contours at $Re = 100$.

$u = 1$ $u = -1$

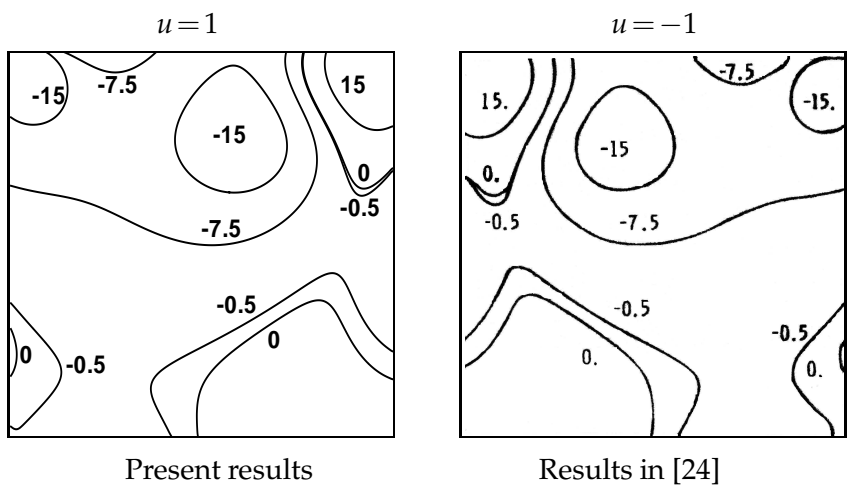Present results   Results in [24]

Figure 7: Contours of the pressure coefficient at $Re = 100$.

packed close to the corner. This is done by the following conformal transformation [28] of independent variables:

$$x = C\xi + \frac{D}{M}[\xi \sinh(2\xi) - \eta \sin(2\eta)],$$

$$y = C\eta + \frac{D}{M}[\eta \sinh(2\xi) + \xi \sin(2\eta)],$$

which transforms the physical plane (x,y) into a computational plane (ξ,η), where $M = \cosh(2\xi) + \cos(2\eta)$. The constants C and D are determined by

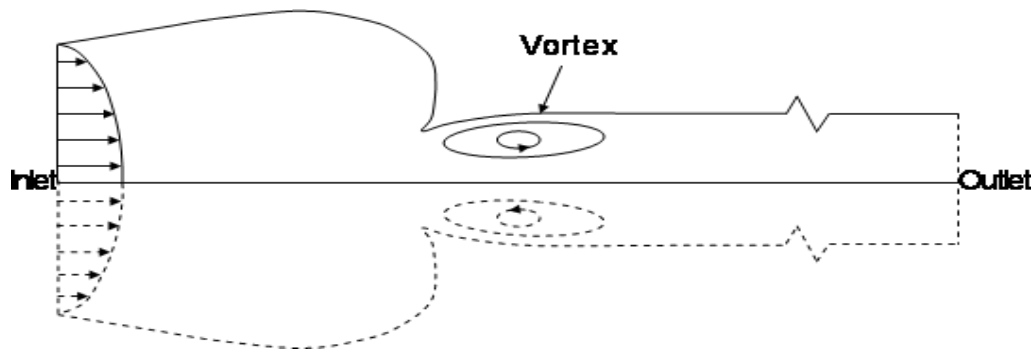$$C = \frac{h_1 + h_2}{2\delta}, \quad D = \frac{h_2 - h_1}{2\delta},$$

Figure 8: Sketch of the constricted channel flow.

where h_1 and h_2 are the inlet and outlet half-widths of the channel and are chosen as 1.0 and 0.5 respectively, while the parameter δ, which controls the smoothness as well as sharpness of the constriction, is chosen in the range of $0 < \delta \leq 1$. This enables us to avoid the coordinate singularity which occurs at $(\xi_0, \eta_0) \simeq (0.56, 1.05)$. Since the whole domain of the channel is given by $-\infty < \xi < +\infty$ and $-\delta < \eta < +\delta$ in the computational space, then $y \rightarrow h_1$ as $x \rightarrow -\infty$ and $y \rightarrow h_2$ as $x \rightarrow \infty$ in the physical space. For the upper half plane, we choose $\eta = \delta$ as the upper boundary and $\eta = 0$ as the symmetric centerline. The choice of the location of the inlet and outlet boundaries affects the flow development, therefore the inlet boundary is set at $x \simeq -7$ and the outlet boundary is set at $x \simeq 14$ far away from the corner. The velocities and pressure at the inlet are given by $u = 1.5(1 - y^2)$, $v = 0$, and p is extrapolated, while zero normal derivative for velocity and zero pressure are imposed at the outlet boundary. Non-slip velocity and zero normal pressure gradient are applied on the upper stationary wall whereas $\partial u / \partial y = 0$, $\partial p / \partial y = 0$ and $v = 0$ are used on the centerline.

Results are presented for three cases, namely $\delta = 0.6$ representing a smooth constricting channel, $\delta = 0.9$ representing a channel with a smooth corner, and $\delta = 1.0$ representing a channel with a smooth but very sharp corner.

Table 2: Separation and reattachment points for $\delta = 0.9$.

Re	Sep.(Present)	Reatt.(Present)	Sep.([26])	Reatt.([26])
175	0.68	0.86	0.66	0.85
200	0.62	1.0	0.62	1.1
250	0.59	1.2	0.57	1.3
500	0.53	2.1	0.52	2.3
600	0.51	2.4	0.51	2.8
750	0.51	3.0	0.51	3.5

In Table 2, the columns 2 and 3 show presently computed separation and reattachment points for a fixed $\delta = 0.9$ at different values of *Re*, while columns 4 and 5 show those
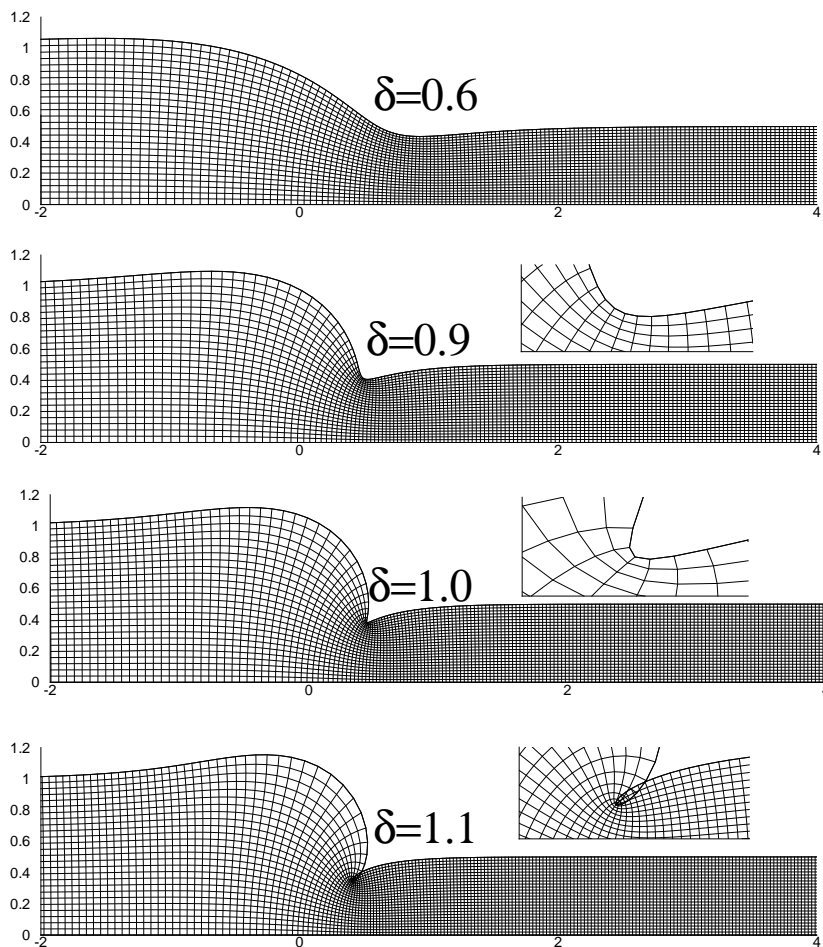
Figure 9: Grid lines for constricted channel with different δ values.

obtained from [26]. It is evident from Table 2 that for small *Re*, the recirculation region is relatively small but becomes large with increasing Reynolds number. It is remarked that no tabulated data was available in the literature to the best of our knowledge. We scanned Fig. 12 of [26] to get the data in Table 2. Therefore, it might be one possible reason for some differences between the two results.

The streamlines in Fig. 10 clearly show the main features of the flow and various separation zones for different δ and Reynolds numbers. For fixed $Re = 250$ and different δ values, we observe that no separation zones appear for $\delta = 0.8$ or less but they start to occur with larger δ. The last two frames in Fig. 10 show that for $\delta = 1.0$ the separation zone becomes larger as the Reynolds number increases. It is therefore concluded that the corner sharpness parameter (δ) and the Reynolds number (*Re*) are two important parameters affecting the development of the corner vortex.
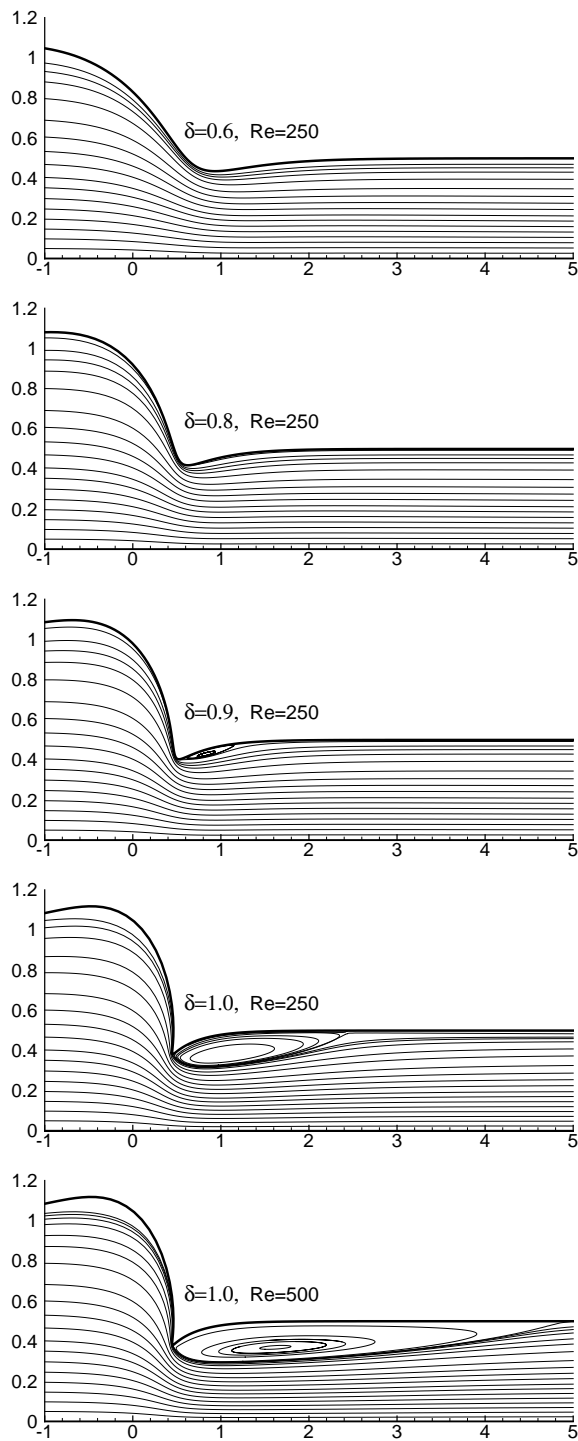
Figure 10: Comparison of streamlines for different geometries and Reynolds numbers.

6 Conclusions

The present paper presents a third-order upwind compact scheme based on flux difference splitting for solving the incompressible Navier-Stokes equations in general curvilinear coordinates using the artificial compressibility method. The accuracy of the numerical scheme is verified by using several benchmark problems. The computed results are in good agreement with available analytical as well as numerical results. Furthermore, the scheme, like its precedent conventional third-order upwind scheme, can be implemented on curvilinear meshes, rendering it a potential for simulating many incompressible flow problems involving complex geometries. Unlike streamfunction-vorticity formulation, the extension of the present scheme to three-dimensional cases is quite straightforward.

Acknowledgments

References

[1] R. S. Hirsh, High order accurate difference solutions of fluid mechanics problems by a compact differencing technique, J. Comput. Phys., 19 (1975), 90-109.
[2] S. K. Lele, Compact finite difference schemes with spectral-like resolution, J. Comput. Phys., 103 (1992), 16-42.
[3] M. Li, T. Tang, B. Fornberg, A compact fourth order finite difference scheme for the steady incompressible Navier-Stokes equations, Int. J. Numer. Meth. Fluids, 20 (1995), 1137-1151.
[4] M. Li, T. Tang, A compact fourth order finite difference scheme for unsteady viscous incompressible flows, J. Sci. Comput., 16(1) (2001), 29-46.
[5] D. V. Gaitonde, J. S. Shang, J. L. Young, Practical aspects of higher-order numerical schemes for wave propagation phenomena, Int. J. Numer. Meth. Eng., 45 (1999), 1849-1869.
[6] D.X. Fu, Y.W. Ma, T. Kobayashi et al., Nonphysical oscillations in numerical solutions: reason and improvement, CFD J., 4(4) (1996), 427-450.
[7] D.X. Fu, Y.W. Ma, A high order accurate difference scheme for complex flow, J. Comput. Phys., 134 (1997), 1-15.
[8] A.I. Tlstykh, M.V. Lipavskii, On performance of methods with third and fifth-order compact upwind differencing, J. Comput. Phys., 140 (1998), 205-232.
[9] X. G. Deng, H. X. Zhang, Developing high-order weighted compact nonlinear schemes, J. Comput. Phys., 165 (2000), 22-44.
[10] A.K. De, V. Eswaran, Analysis of a new high resolution upwind compact scheme, J. Comput. Phys., 218 (2006), 398-416.
[11] P. L. Roe, Approximate Riemann solvers, parameter vectors, and difference scheme, J. Comput. Phys., 43 (1981), 357-372.

[12] A. J. Chorin, A numerical method for solving incompressible viscous flow problems, J. Comput. Phys., 2 (1967), 12-26.

[13] S. E. Rogers, D. Kwak, Upwind differencing for the time-accurate incompressible Navier-Stokes equations, AIAA J., 28(2) (1990), 2253-62.

[14] S. E. Rogers, D. Kwak, An upwind differencing scheme for the incompressible Navier-Stokes equations, Appl. Numer. Math., 8 (1) (1991), 43-64.

[15] D. Choi, C. L. Merkle, Application of time-iterative schemes to incompressible flow, AIAA J., 23 (1985), 1518-1524.

[16] P. M. Hartwich, C. H. Hsu, An implicit flux-difference splitting scheme for 3D incompressible N-S solutions to leading edge vortex flow, AIAA paper (1986) 86-1839.

[17] L. Yuan, Comparison of implicit multigrid schemes for three dimensional incompressible flows, J. Comput. Phys., 177 (2002), 134-155.

[18] R. Beam and R. F. Warming, An implicit scheme for the compressible Navier-Stokes equations, AIAA J., 16 (1978), 393-402.

[19] T. M. Shih, C. H. Tan, B. C. Hwang, Effects of grid staggering on numerical scheme, Int. J. Numer. Meth. Fluids, 9 (1989), 193-212.

[20] F. Wang, Rizwan-uddin, A modified nodal scheme for the time-dependent, incompressible Navier-Stokes equations, J. Comput. Phys., 187 (2003), 168-196.

[21] T. C. Papanastasiou, G. C. Georgiou, A. N. Alexandrou, Viscous Fluid Flow, CRS press, 1999.

[22] S. Garcia, The lid-driven square cavity flow from stationary to time periodic and chaotic, Commun. Comput. Phys., 5(2) 2007, 900-932.

[23] U. Ghia, K. N. Ghia, C.T. Shin, High *Re* solutions for incompressible Navier-Stokes equations, J. Comput. Phys., 49 (1983), 387-411.

[24] F. Sotiropoulos, S. Abdallah, Coupled fully implicit solution procedure for the steady incompressible Navier-Stokes equations, J. Comput. Phys., 87 (1990), 328-348.

[25] Y. X. Ren, M. Liu and H. Zhang Implementation of the divergence-free and pressure-oscillation-free projection method for solving the incompressible Navier-Stokes equations on the collocated grids. Commun. Comput. Phys., 2 (2007), 746-759.

[26] S. K. Pandit, J. C. Kalita, D. C. Dalal, A fourth-order accurate compact scheme for the solution of steady Navier-Stokes equations on non-uniform grids, Comput. Fluids, (2007), in press.

[27] P. F. A. Mancera, A study of a numerical solution of the steady two dimensions Navier-Stokes equations in a constricted channel problem by a compact fourth order method, Applied Mathematics and Computation, 146 (2003), 771-790.

[28] P. F. A. Mancera, R. Hunt, Fourth-order method for solving the Navier-Stokes equations in a constricting channel, Int. J. Numer. Meth. Fluids, 25 (1997), 1119-1135.